Title

Synthetically non-Hermitian nonlinear wave-like behavior in a topological mechanical metamaterial.

Journal

Proceedings of the National Academy of Sciences of USA, 120(18)

Authors

Xiu, Haning

Frankel, Ian

Liu, Harry

et al.

Publication Date

2023-05-02

DOI

10.1073/pnas.2217928120

Peer reviewed

PNAS RESEARCH ARTICLE | ENGINEERING

Synthetically non-Hermitian nonlinear wave-like behavior in a topological mechanical metamaterial

Haning Xiu[a,b,1], Ian Frankel[b,1], Harry Liu[c,1], Kai Qian[b], Siddhartha Sarkar[c], Brianna MacNider[b], Zi Chen[a,2], Nicholas Boechler[b,2], and Xiaoming Mao[c,2]

Edited by Glaucio Paulino, Princeton University, Princeton, NJ; received October 20, 2022; accepted March 20, 2023, by Editorial Board Member Yonggang Huang

Topological mechanical metamaterials have enabled new ways to control stress and deformation propagation. Exemplified by Maxwell lattices, they have been studied extensively using a linearized formalism. Herein, we study a two-dimensional topological Maxwell lattice by exploring its large deformation quasi-static response using geometric numerical simulations and experiments. We observe spatial nonlinear wave-like phenomena such as harmonic generation, localized domain switching, amplification-enhanced frequency conversion, and solitary waves. We further map our linearized, homogenized system to a non-Hermitian, nonreciprocal, one-dimensional wave equation, revealing an equivalence between the deformation fields of two-dimensional topological Maxwell lattices and nonlinear dynamical phenomena in one-dimensional active systems. Our study opens a regime for topological mechanical metamaterials and expands their application potential in areas including adaptive and smart materials and mechanical logic, wherein concepts from nonlinear dynamics may be used to create intricate, tailored spatial deformation and stress fields greatly transcending conventional elasticity.

metamaterials | topology | mechanics | nonlinearity | non-Hermitian

Significance

By tailoring the structure that forms materials, unusual properties and functions are being programmed into an ever-growing collection of "mechanical metamaterials." Within this material scope, "Maxwell lattices" have received particular interest due to their reconfigurability and topologically protected soft deformation modes and stress states. Here, we go beyond the linear formulism currently used to study Maxwell lattices and reveal how the interplay between topological states and nonlinearity leads to fascinating deformation patterns beyond conventional elasticity. We further show that the static spatial deformation of 2D Maxwell lattices maps onto space-time waves in a 1D non-Hermitian (active), nonreciprocal system. This establishes a way to tailor stress and strain in materials and sets tantalizing questions regarding the dynamics of such metamaterials.

The study of topological band theory in condensed matter physics has led to novel classes of materials termed topological insulators (1, 2) and topological superconductors (3), which support localized modes at the materials' edges that are highly robust to defects and perturbation (4). The stability of these modes stems from topological protection conferred by the material's bulk properties. Topologically nontrivial materials have been shown to support unidirectional, backscattering-immune mode propagation, thus facilitating the development of new superconducting devices (5) with applications in areas such as quantum computation (6, 7) as well as magnetoelectronic (8) and optoelectronic devices (9). Recently, the topological band theory has also been applied to the mechanical domain, which has enabled the creation of topological mechanical metamaterials (TMMs) that support phenomena such as energy localization and immunity to backscattering at finite frequencies and a new ability to design and control quasi-static and spatiotemporally varying stress and deformation fields in materials (10–14).

Topological mechanical metamaterials at the Maxwell point (as shown in Fig. 1*A*), where the number of degrees of freedom (DOFs) balances with the number of constraints in the bulk, are a subclass of TMMs (referred to as "Maxwell lattices") in which modes having zero energy, which are referred to as "zero" or "floppy" modes (ZMs), arise. Such zero energy modes allow the lattice to deform without an energy cost. These ZMs have a topological nature described by a polarization vector that is analogous to the topological invariant seen in the Su–Schrieffer–Heeger model (15), and they localize such that, in the linkage-limit, the edges the polarization vector points toward have zero stiffness and the opposite edges are rigid (infinite stiffness) (16). The direction of the polarization vector is controlled by the lattice's geometry and is tunable through a homogeneous zero energy deformation, also called the Guest–Hutchinson mode, and it is intrinsic to the lattice (17). In the presence of interfaces or topological defects, this polarization can result in internal localized states of self-stress (SSSs, which refers to force-balanced stress eigen-states) and ZMs (16, 18). Further, due to the balanced numbers of DOFs and constraints in the bulk, such lattices are holographic, and the state of the zero-energy configuration of a $d-$dimensional material can be fully prescribed from its $(d-1)$ dimensional boundary. In special cases such as twisted kagome lattices, the mechanisms can be written as conformal transformations (19, 20). Such holography adds additional levels of deformation control since the bulk state can be controlled at the boundary via zero-energy configurations.

The authors declare no competing interest.

This article is a PNAS Direct Submission. G.P. is a guest editor invited by the Editorial Board.

[1]H.X., I.F., and H.L. contributed equally to this work.

[2]To whom correspondence may be addressed. Email: zchen33@bwh.harvard.edu, nboechler@eng.ucsd.edu or maox@umich.edu.

This article contains supporting information online at http://www.pnas.org/lookup/suppl/doi:10.1073/pnas.2217928120/-/DCSupplemental.

Published April 24, 2023.

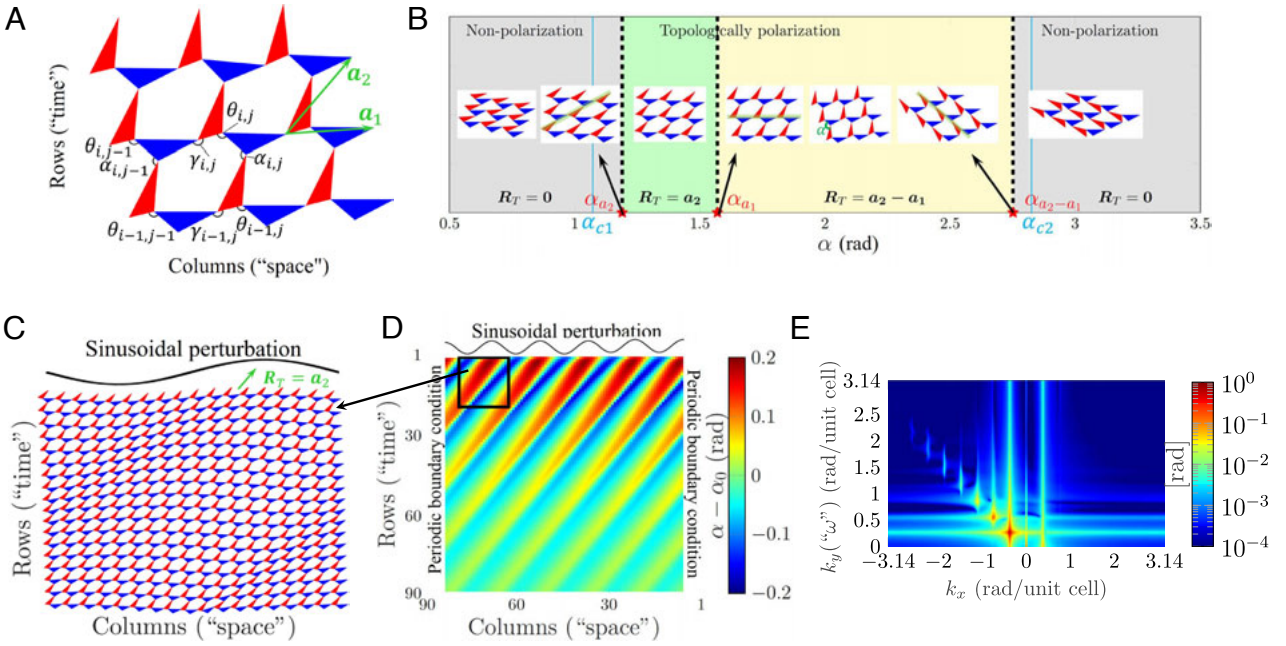

Fig. 1. The 2D zero energy deformation fields in static Maxwell lattices map onto waves in 1D non-Hermitian, nonreciprocal dynamical systems and rich nonlinear phenomena emerge. The axes labels denote the mapped quantities. (*A*) Geometry of the deformed kagome lattice we study here, where θ, α, and γ are internal angles between the red and blue triangles in the unit cells (with normalized dimensionless side lengths of (0.4, 0.8, 1) and (0.5, 0.7, 1) for red and blue triangles, respectively). (*B*) Topological transitions of the lattice shown in (*A*) by twisting α. The black arrows point to configurations at the boundary between polarization domains. The blue vertical lines denote angles between which $\det \epsilon_0 < 0$ and the linearized ZM deformation of the homogeneous lattice obeys hyperbolic PDEs, outside of which $\det \epsilon_0 > 0$ and the lattice obeys elliptic PDEs. (*C*) A zoomed-in view of a calculated section of an initially homogeneous lattice with $\mathbf{a_2}$ polarization, $\alpha_0 = 1.3344$, and periodic boundary conditions on the left and right, perturbed by a sinusoidal static signal with $k_X = 0.349$ rad/unit cell and $\varepsilon = 20$ mrad. (*D*) Full lattice corresponding to the section shown in (*C*). (*E*) 2D Fourier transform of the deformation field shown in (*D*), where the nonlinear phenomena of harmonic generation can be seen. Subscripts *x* and *y* denote the "columns" and "rows" axes, respectively.

Due to their intrinsic scalability and a high degree of control over deformation and stress fields through the tuning of the topological polarization vector, Maxwell lattices have been suggested for future use related to robotics, impact and energy absorption, tear resistance, nanoscale manufacturing via origami, and acoustic and phonon logic and computation devices, e.g., logic strategies via multistable metamaterials (21–27).

Although this revealed wealth of applications, the study of Maxwell lattices has been confined, by and large, to the linear, small deformation limit (16, 17, 20, 28, 29). Intriguing nonlinear effects such as topological solitons (which are localized transitions between two topologically different states) have been revealed in one-dimensional (1D) Maxwell chains (30, 31). In two-dimensional (2D) topological Maxwell lattices, the study of nonlinear effects has been so far limited to perturbation theories (22). This is an important gap as nonlinear systems do not obey superposition and, as such, support an ability to control the spatiotemporal allocation of energy in materials that vastly exceeds their linear counterparts (32–34) through phenomena such as self-localization (35, 36), frequency conversion and dynamic tunability (37, 38), and chaos (39), as well as rich interplay with finite-frequency topological states (2, 22, 40–45). The nonlinear response of topological systems has been extensively studied within the realm of photonics, including experimental demonstrations involving frequency conversion, edge solitons, and active lasing (41). Within the context of mechanical topological systems, a handful of experiments in 1D have demonstrated phenomena such as nonlinear conduction via topological solitons (30, 46) and topological phase transitions (47). Hence, we envision that combining nonlinear responses with topological nontriviality (and its characteristic localization and amplification, nonreciprocity, and robust protected states) will lead to an important expansion of the ability to tailor spatiotemporal stress, deformation, and energy fields, with application areas demonstrated for nonlinear dynamical systems ranging from impact mitigation (48) to neuromorphic (49) and ultrafast mechanoacoustic computation (50, 51).

In this work, we show that ZMs of 2D topological Maxwell lattices map to waves in 1D non-Hermitian active or damped systems, which have been shown to exhibit unique phenomena such as parity–time symmetry and unidirectional invisibility (52, 53) and nonreciprocal, i.e., the response is asymmetric when source and observation points are interchanged (54–56) dynamical systems, which maps the 2D elastic deformation in TMMs to 1D nonlinear wave propagation. This mapping shares similarity with the symplectic elasticity method that takes one spatial direction (e.g., the transverse direction) as a pseudotime variable and reduces the total spatial dimensions (57–59). A rich set of nonlinear phenomena associated with dynamical systems arise in this static system, offering precise remote control of complex zero-energy spatial deformation patterns. It is important to highlight that there is a direct interplay between the topology of the lattice, which directly maps to the synthetic non-Hermiticity, and the observed nonlinear phenomena as a result of the topology-induced amplification. As such, small perturbations can lead to large amplitude, nonlinear responses. In other fields, space-time mappings have historically brought critical insight in many fields in science, from polymer physics to quantum criticality, and time crystals (60–63). Using exact geometric calculations and subsequent experimental validation of nonlinear ZMs in deformed kagome TMMs, we observe spatial nonlinear wave-like phenomena including harmonic generation, localized

topological domain switching, amplification-enhanced frequency conversion, and solitary waves. The results presented here are scale-free, material independent, and add a unique dimension to mechanical metamaterials engineering, wherein deformation fields can be predicted and intricately designed using insights derived from the analysis of nonlinear waves in non-Hermitian systems (32, 35, 52, 64–67).

Results

Topological Polarization and Analogy to 1D Dynamical Systems. In Maxwell lattices, the number of DOFs and the number of constraints are identical in the bulk. By the Maxwell–Calladine index theorem (16, 19, 28, 68), this equality indicates that the difference between the number of ZMs (zero modes) and SSSs (states of self-stress) is proportional to the size of the open boundary. By manipulating the unit cell geometry, the ZMs can be localized at the boundaries of the lattice at which the topological polarization vector $\mathbf{R}_T$ points. Considering a finite 2D deformed kagome lattice consisting of N_x (number of columns) by N_y (number of rows) unit cells (with two triangles per unit cell), the total number of nodes and bonds (edges of triangles) under open boundary conditions are $N = 3N_xN_y + N_x + N_y$ and $N_b = 6N_xN_y$, respectively. Consequently, the number of ZMs N_0 is given by $N_0 = 2N - N_b + N_s = 2N_x + 2N_y + N_s$, where N_s are the number of SSS in the system, with $N_s = 0$ for an open boundary conditioned lattice. Removing the number of rigid body DOFs of the whole lattice, the remaining number of nontrivial ZMs is $2N_x + 2N_y - 3$. For our lattice, shown in Fig. 1*A*, its configuration is described by a set of angles $\{\alpha_{i,j}, \theta_{i,j}, \gamma_{i,j}\}$ defined for each unit cell at the i-th row and j-th column. The counting of ZMs and the definition of every angle in the lattice are described in *SI Appendix*, Note 1. For a homogeneous lattice, all $\{\alpha_{i,j}, \theta_{i,j}, \gamma_{i,j}\}$ are set to be the same in each unit cell, leaving only one free angle α (i.e., the Guest–Hutchinson mode, which homogeneously transforms the whole lattice without costing elastic energy) to determine the geometry of the homogeneous configuration as is shown in Fig. 1*B*. This angle also determines the topological polarization $\mathbf{R}_T$ of the lattice (16), which is defined via the phase winding $\phi(k)$ of the determinant of the equilibrium matrix $\mathbf{Q}$ that maps tension on the bonds to the total force on the sites in momentum space k, where $[\mathbf{Q}(\mathbf{k}) = |\mathbf{Q}(\mathbf{k})|^{i\phi(\mathbf{k})}]$, and lattice vectors $\mathbf{a}_i$, such that $\mathbf{R}_T = \sum_i a_i \frac{1}{2\pi} \oint dk_i \cdot \nabla_{k_i} \phi(k)$. When $\mathbf{R}_T = 0$ (with a proper gauge), all edges of the lattice have ZMs, while when $\mathbf{R}_T \neq 0$, the polarization vector points toward the "soft" edges that the ZMs are localized to, such that the edges opposite to the direction of $\mathbf{R}_T$ becomes the "hard" edges. As shown in Fig. 1*B*, the deformed kagome lattice experiences topological transitions at three critical angles $\alpha_{\mathbf{a_2}}$, $\alpha_{\mathbf{a_1}}$, and $\alpha_{\mathbf{a_2}-\mathbf{a_1}}$. When $\alpha < \alpha_{\mathbf{a_2}}$ or $\alpha > \alpha_{\mathbf{a_2}-\mathbf{a_1}}$, the lattice has $\mathbf{R}_T = 0$. Between these two critical angles, the lattice is topologically polarized, and $\mathbf{R}_T$ has two distinct directions, $\mathbf{a_2}$ or $\mathbf{a_2} - \mathbf{a_1}$, separated by α_{a_1}.

We first consider the deformation of our TMMs in the continuum limit, where ZMs are determined at linear order of the x displacement vector, u_x, by the third order partial differential equation (PDE):

$$([\epsilon_{0yy}\partial_x^2 - 2\epsilon_{0xy}\partial_x\partial_y + \epsilon_{0xx}\partial_y^2] + [C_1\partial_x^3 + C_2\partial_x^2\partial_y + C_3\partial_x\partial_y^2])u_x = 0, \quad [1]$$

with ϵ_0 being the Guest–Hutchinson mode, a soft strain always present in Maxwell lattices (69) (*SI Appendix*, Note 3 for the derivation of Eq. **1**, its interpretation as a wave equation in 1D, as well as a discussion of time reversal symmetry and energy conservation of this wave equation). As discussed in ref. 17, this type of soft, spatially varying modes u generally arise in all materials in which a homogeneous strain ϵ_0 is soft. In Maxwell lattices, this soft strain ϵ_0 is guaranteed to exist and cost exactly zero energy (69), and the spatially varying soft modes u take the form of exact zero energy modes, protected by the Maxwell–Calladine index theorem (17, 20). Such soft strain ϵ_0 can also accidentally arise due to geometric singularities in overconstrained lattices, such as planar quadrilateral kirigami, where these soft modes u cost a small amount of elastic energy even when the hinges are considered perfect (70–74). Importantly, in Maxwell lattices, the fact that these ZMs are exact zero energy makes them scale-free and materials-independent.

Solutions to this PDE to the quadratic order (first square brackets) can be obtained by considering the case with prescribed k_x (wave number along x), where the ZM is given by $k_y = \frac{\epsilon_{0xy} \pm \sqrt{-\det\epsilon_0}}{\epsilon_{0xx}} k_x$. When $\det\epsilon_0 > 0$, corresponding to the Guest–Hutchinson mode being a dilation dominant (auxetic) mechanism and the PDE being elliptic, k_y is complex with an imaginary part $k_y'' \propto \pm k_x$, describing a pair of ZMs localized on the top and bottom edges, respectively. With proper coordinate transformations, these ZMs are mapped to conformal transformations (17, 19). Adding terms with higher-order derivatives only quantitatively changes these ZMs. In the opposite case, $\det\epsilon_0 < 0$, corresponding to the Guest-Hutchinson mode being a shear dominant (nonauxetic) mechanism and the PDE being hyperbolic, k_y is real, describing a pair of bulk ZMs. Unless fine-tuned, when terms of higher-order derivatives (the second square brackets in Eq. **1**) are introduced, the solution of k_y becomes complex, with the imaginary part $k_y'' \propto k_x^2$ being higher order, indicating slower decay. Importantly, the sign of these decay rates is determined by the topological polarization $\mathbf{R}_T$, in all cases. The same conclusion can be reached by starting with given k_y. We note that most known cases of topologically polarized 2D Maxwell lattices belong to the hyperbolic case ($\det\epsilon_0 < 0$) (17).

For the nonauxetic case, the mapping to a hyperbolic equation suggests that an analogy can be made between the 2D spatial PDE of Eq. **1** and a 1D space-time PDE (more details in *SI Appendix*, Note 3, Eqs. S.32–S.35). As shown in Fig. 1, the specific analogy between 2D spatial deformation and 1D spatiotemporal deformation we propose herein has progression across columns, or in the x direction, correlating with space, and progression across rows, or in the y direction, correlating with time evolution in the 1D analog dynamical system ($y \leftrightarrow t$). In Eq. **1**, the second-order cross-derivative term thus provides a conservative nonreciprocity along the x direction as the "waves" propagate in "time" (y). Interestingly, the third-order terms become nonconservative in the analog system, making the wave equation "synthetically" non-Hermitian (53). The y-component of the topological polarization in the 2D spatial lattice thus translates to a spatially uniform activity/damping in the 1D space-time lattice. Similarly, the $\partial_x\partial_y^2 u_x$ term provides a nonreciprocal activity in the effective 1D lattice.

Given the aforementioned analogy to a 1D nonreciprocal, non-Hermitian, spatiotemporal system, we aim to study "wave propagation" in our 2D spatial TMM. With the expected polarization-dependent spatial amplification/decay, we expect large amplitude deformations outside the confines of a linear, small deformation approximation, leading to the proliferation of rich nonlinear phenomena. We note that while the spatiotemporal analogy is made using Eq. **1**, which is linear, the full deformation field can be described by adding nonlinear

terms, such that the mapping between the topological phase and the synthetic non-Hermiticity still applies in the nonlinear regime. To this end, we numerically calculate the exact nonlinear ZM configuration for chosen homogeneous configurations, with periodic boundary conditions on its left and right edges, and then an applied perturbation to the soft or hard edge of the lattice such that the θ angles $\theta_{1,j} = \theta_0 + f(j)$, where θ_0 is the initial homogeneous θ value. Given three angles and fixed edge lengths of the triangles, a hexagon is fully determined to within a choice of a single convex or concave angle (Fig. 1; *SI Appendix*, Note 2, Eqs. S.2–S.5 for details). We choose the convexity where the complementary angle (angle on the opposite side across the hinge) to θ is always less than π, which allows us to span the entire topological polarization range. By solving iteratively through each row starting with the edge where the perturbation is applied, the entire lattice can be determined geometrically, without approximation. Periodic boundary conditions are implemented by using Newton's method and numerically solving for a compatible periodic solution at each row (*SI Appendix*, Note 2, Eqs. S.13 and S.14). Within the context of our analogy to a 1D spatiotemporal system, this is as if we are applying an initial condition across the entire lattice and then letting the system evolve in time.

Linear and Weakly Nonlinear Response. We start by verifying wave characteristics of ZMs in 2D Maxwell lattices in the linear and weakly nonlinear regimes using our exact geometrical numerical method. Because the lattice satisfies the Maxwell criterion, this ZM configuration is exactly geometrically determined, independent of materials and length scales, in contrast to low-energy modes studied in refs. 70, 72–74. We start with a homogeneous lattice deep in the $\mathbf{a_2}$ topologically polarized phase. The critical angles between which the lattice is hyperbolic, α_{c1}, α_{c2}, are shown in Fig. 1*B*. We then apply a low-amplitude sinusoidal perturbation to the soft edge (the top row), such that $f(j) = \varepsilon \sin(k_x j)$. The resulting deformation field is shown in Fig. 2 *A*–*C* and is described by a superposition of two ZMs that decay into the bulk that closely match expectations from the linear theory (further described in *SI Appendix*, Note 2 and Fig. S4). A 2D Fourier transform of the deformation field can be seen in Fig. 2*B*, overlaid with two white lines denoting the real part of the wave number k_y of the two ZMs predicted by the linear theory. Of the two ZMs, one has a shorter y-direction wavelength (higher "frequency" in the effective 1D spatiotemporal system) with faster decay, which is part of a highly dispersive branch, and the other a longer y-direction wavelength with slower decay, which is part of a weakly dispersive branch. The initial increase in amplitude of the deformation field with distance from the perturbation (decreasing row number) that can be seen in Fig. 2 *A* and *C* is due to the input phase of the two ZMs and coherent interference. There are two superimposed, phase-shifted oscillating modes with different values of vertical wavevector component k_y, whose envelopes decay exponentially downward from the top, each at different rates. The combination of the differing input phase and different decay rates of the two ZMs results in the rapid change in the amplitude of α from the top surface into the bulk. Fig. 2 *D*–*F* details the same system shown in Fig. 2 *A*–*C*, but with a larger initial perturbation, inducing the nonlinear phenomena of harmonic generation (38), similar to Fig. 1. An additional example that verified the linear and weakly nonlinear results of a lattice in the $\mathbf{a_2} - \mathbf{a_1}$ polarized phase can be found in *SI Appendix*, Note 4.

These static ZMs in 2D, which resemble spatiotemporal patterns of 1D dynamical systems, are accurately described by the PDE Eq. **1**, the coefficients of which are determined by the unit cell geometry. For a given k_x, two solutions of complex k_y arise from the PDE (dashed lines in Fig. 2 *B* and *E*)), which agree well

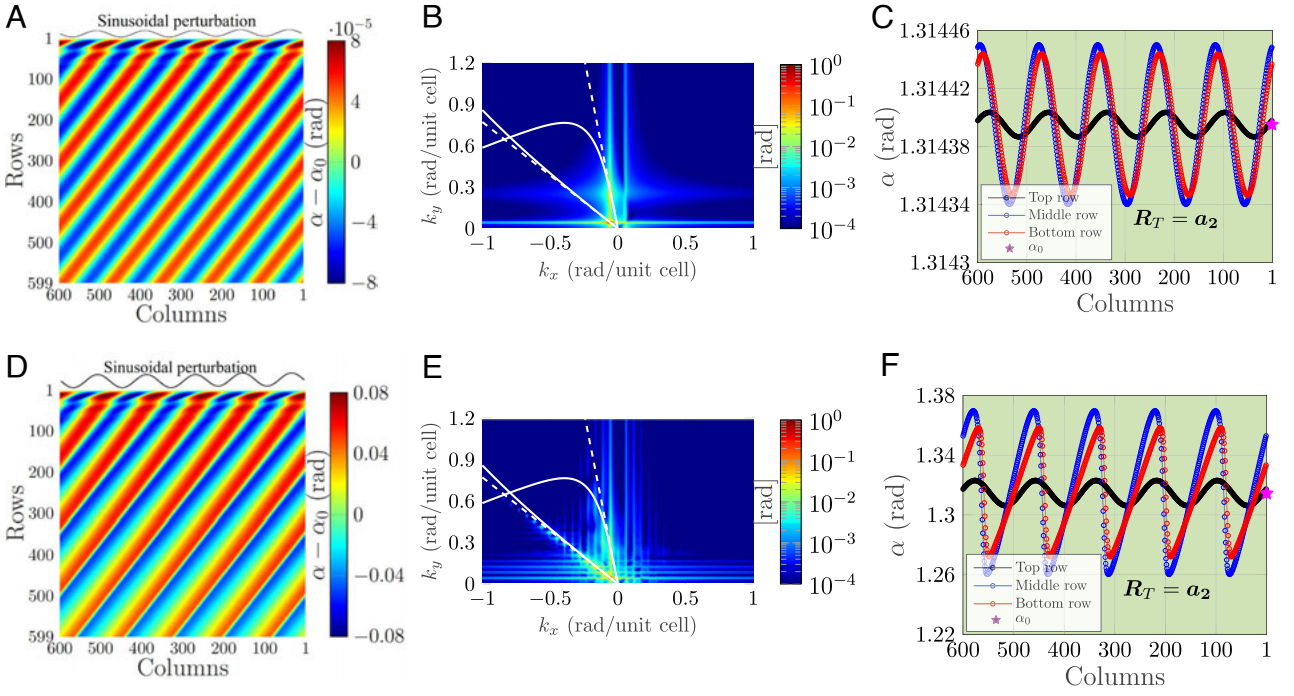

Fig. 2. Linear and weakly nonlinear response due to a sinusoidal perturbation applied to the soft (*Top*) edge of a kagome Maxwell lattice deep in the $\mathbf{a_2}$ polarized region. The lattice has $\alpha_0 = 1.3144$ rad and $k_x = 0.0524$ rad/unit cell. (*A*–*C*) Linear response at $\varepsilon = 1$ μrad. (*D*–*F*) Weakly nonlinear response and harmonic generation at $\varepsilon = 1$ mrad. (*A* and *D*) Deformation field. (*B* and *E*) 2D Fourier transform of (*A* and *D*). White solid lines denote the real part of the ZMs predicted by linear theory, and white dashed lines represent the real parts solved from the PDE Eq. **1**. (*C* and *F*) Select rows of (*A* and *D*). The pink star in (*C* and *F*) denotes the initial homogeneous angle, and the background shading denotes the topological phase (always a_2 polarization in this case).

with both the values computed using the full lattice linear theory (solid curves) and the geometric numerical calculation (heat map). Further comparisons including the whole wavefield are included in *SI Appendix*, Note 3. These agreements demonstrate the quantitative link between ZMs in 2D Maxwell lattices and 1D dynamical systems.

Strongly Nonlinear Phenomena. We now proceed to explore more strongly nonlinear phenomena arising in these lattices. In particular, we show three examples, namely, automatic and localized topological polarization switching, amplification-enhanced frequency conversion, and solitary wave formation. The first example, the switching of topological polarization as a result of nonlinear waves, occurs when the lattice is in the $\mathbf{a_2}$ phase close to the boundary with the $\mathbf{a_2} - \mathbf{a_1}$ phase. As shown in Fig. 3, for this case, a sinusoidal perturbation causes regions of deformation significant enough to cause local transitions to $\mathbf{a_2} - \mathbf{a_1}$ polarization. The boundaries between regions of different polarization are known to support internal SSSs (18), which has been shown to have implications for lattice fracture (75). We highlight that this domain switching is a strictly nonlinear effect as it requires finite deformation. Such finite deformation effects may lead to boundary-defined (holographic) programmable topological domain walls.

The second example, amplification-enhanced frequency conversion, occurs when the lattice is excited from the hard edge of a polarized lattice or either edge of a nonpolarized lattice. In the case of perturbing from the hard edge, following the linear theory, we expect the perturbation to project to two ZMs, which both grow exponentially into the bulk. In the context of our analogy with the 1D, nonreciprocal, non-Hermitian system, this would map to either an active system evolving forward in time or a damped system evolving backward in time. In Fig. 4 *A*–*C*, we show the calculation for the sinusoidal perturbation of a lattice deep in the $\mathbf{a_2} - \mathbf{a_1}$ domain. As shown in Fig. 4*A*, the deformation field amplifies into the bulk. We stop the calculation at 18 rows, after which a zero strain solution cannot be found due to overlap or nonconnection of the triangles such that the lattice is "broken." To better illustrate the "time evolution" of the mode, we show the trajectory of the lattice in the phase space of the angles. In Fig. 4 *A* and *C*, the growth in amplitude can be seen to be accompanied by the generation of higher-frequency wave components, which is connected to the blue loops in the angular phase space plot of Fig. 4*B*.

The other case where the ZM amplifies is when a nonpolarized lattice is perturbed from either edge. In this case, in the linear theory, one ZM grows and the other decays. A generic perturbation projects to both ZMs, and the growing one is observed far from the edge. Here, we study a sinusoidal perturbation on a lattice deep in the $\mathbf{R}_T = 0$ domain. As mentioned above, linear ZMs in this lattice are described by conformal transformations. In Fig. 4 *D*–*F*), using the same conventions as Fig. 4 *A*–*C*), we show the deformation of the perturbed lattice. In contrast to the hyperbolic case of hard-edge perturbation, in Fig. 4 *D* and *F*, we see the formation of "kinks." At linear order, these kinks can be understood as a signature of conformal transformations, which have a one-to-one correspondence with complex analytic functions. All analytic functions periodic in x can be expanded in the basis of e^{ikz}, which features these kinks. Higher-order terms, both in u and in derivatives, lead to further complex features of these kinks. Such kink formation may find future use in applications that can take advantage of deformation amplification or stress concentration. In *SI Appendix*, Note 5 and Fig. S7, we show further examples for sinusoidal perturbation of $\mathbf{R}_T = 0$ and $\mathbf{a_2}$ lattices that are closer to the polarization boundaries, wherein domain switching can be observed.

The third—and perhaps the most intriguing—example, solitary waves, occurs when the lattice is subject to localized perturbations. Typically described as localized waves that maintain their shape as they propagate with constant, often amplitude-dependent, speed and shape, solitary waves are one of the most canonical phenomena that emerge from nonlinear systems (34–36). Herein, we distinguish solitary waves from the more restrictive localized type of wave referred to as "solitons," which "reappear virtually unaffected in size or shape" following collisions (76). While solitary waves are most commonly considered in conservative systems, they have also been studied in a wide range of nonconservative (i.e., non-Hermitian) systems (32, 34, 35, 52, 64, 66, 67).

To explore the possibility of such localized traveling structures in our system, we induce a point perturbation at the top of a lattice with the same homogeneous configuration as studied in Fig. 2 and sweep a range of perturbation amplitudes, where $f(j) = \varepsilon\delta(j - j_p)$ and j_p is the column to which the perturbation is applied. As can be seen in Fig. 5 *A*–*C*), using the language of the 1D spatiotemporal system analogy, we see that two main solitary waves emerge with nearly constant speeds and interact with each other: one with a fast wave-speed and decay rate and the other with a slow wave-speed and decay rate. In Fig. 5 and below, we use

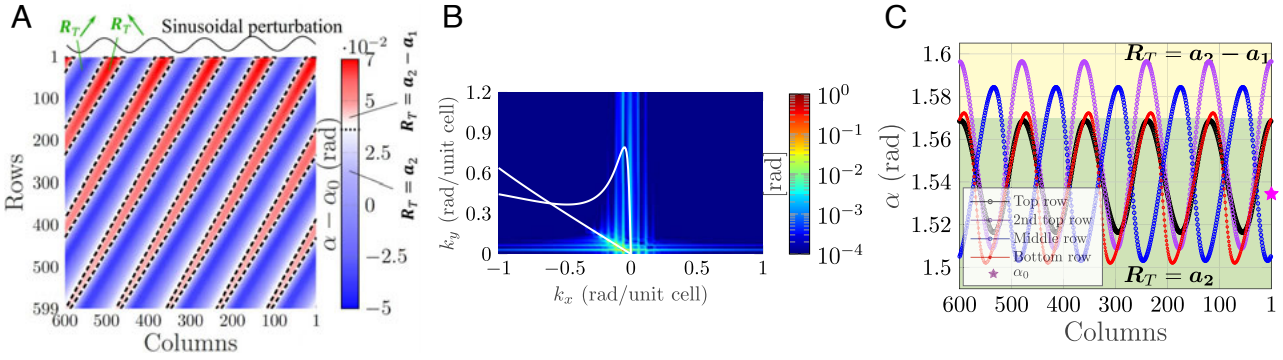

Fig. 3. Intrinsic localized topological polarization switching (a strictly nonlinear phenomenon) and domain formation due to a sinusoidal polarization applied to the soft edge (*Top*) of the deformed kagome Maxwell lattice near the border of the $\mathbf{a_2}$ polarized phase. The lattice has $\alpha_0 = 1.5344$ rad, $k_x = 0.0524$ rad/unit cell, and $\varepsilon = 1$ mrad. (*A*) Deformation field, (*B*) 2D Fourier transform of (*A*) with white lines representing the real part of the ZMs solved from the linear theory, and (*C*) select rows of (*A*). The pink star in (*C*) denotes the initial homogeneous angle, and the background shading denotes the topological phases. The dashed black lines in (*A*) denote boundaries between regions of different polarizations.

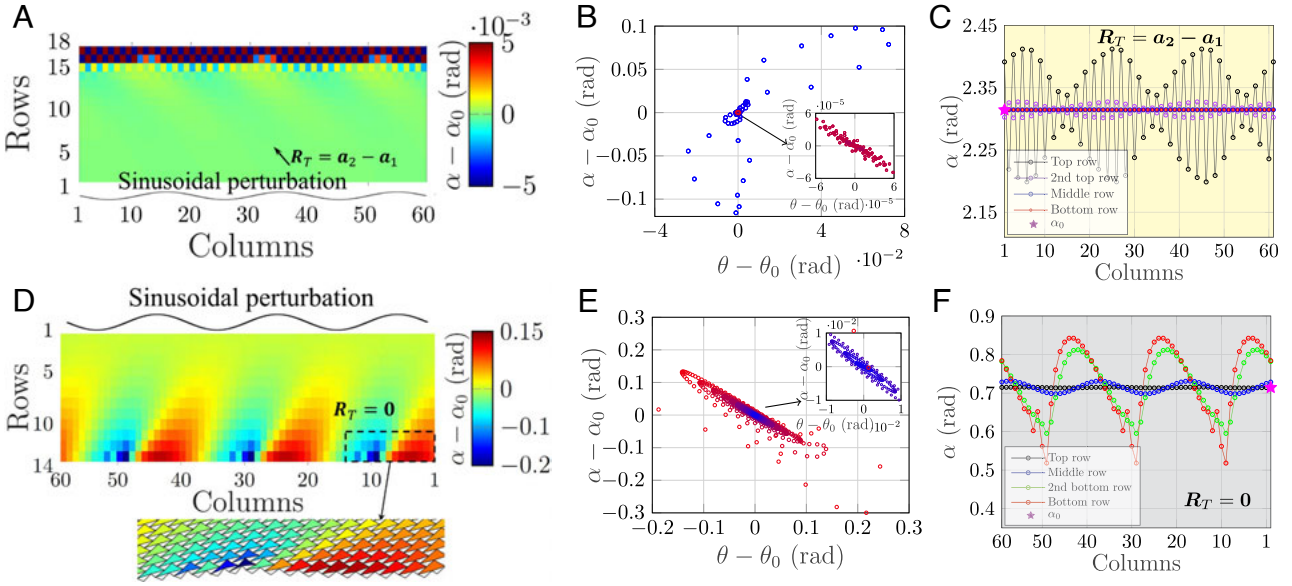

Fig. 4. Nonlinear wave amplification and frequency conversion in Maxwell lattices in response to sinusoidal perturbation, wherein the topological localization (and equivalently "synthetic non-Hermiticity") drives large amplitude, nonlinear deformations. (*A–C*) Hard-edge perturbation (from the *Bottom*) of an $\mathbf{a_2 - a_1}$ polarized lattice ($\alpha_0 = 2.3144$ rad), where $k_x = 0.314$ rad/unit cell and $\varepsilon = 1$ μrad. (*D–F*) Perturbation (from the *Top*) of an unpolarized lattice with $\alpha_0 = 0.7144$ rad, with $k_x = 0.314$ rad/unit cell and $\varepsilon = 1$ mrad. (*A* and *D*) Deformation field. The configuration of the lattice in the dashed box is shown below the plot. (*B* and *E*) Phase space of (*A* and *D*), where blue to red color gradient denotes a progression from *Top* to *Bottom* rows, respectively. The insets provide a zoomed-in view near the perturbation. (*C* and *F*) Select rows of (*A* and *D*). The pink stars in (*C* and *F*) denote the initial homogeneous angles, and the background shadings denote the polarization regions.

r and c to denote rows and columns, respectively, in the derivative terms. Fig. 5 *D* and *E* shows the dependence of speed and decay rate of the two solitary waves on perturbation amplitude. At first glance, it appears that there is a minimal interaction between the two solitary waves as they intersect. However, additional calculations for the same conditions as described in Fig. 5, but with five times fewer columns, and thus more collisions between the waves (*SI Appendix*, Note 6), show a significantly greater variation in the speeds and decay rates of the solitary waves. This suggests that the two solitary waves do interact upon their collisions. Additional data for the peak-to-peak decay rate in terms of α and the evolution of average α with an increasing row number are included in *SI Appendix*, Fig. S9. Interestingly, both the narrow and wide lattices have perturbation amplitudes for which the decay rate of α is zero across the sampled rows (in contrast to $d^2\alpha/dr^2$), which is reminiscent of solitary waves in nonconservative systems, where nonlinearity, dispersion, and loss/gain balance to form a traveling wave packet of constant shape (34, 35, 52, 66, 67). Such slow decay suggests that these waves can be considered analogs to weakly dissipative solitary waves (64, 67).

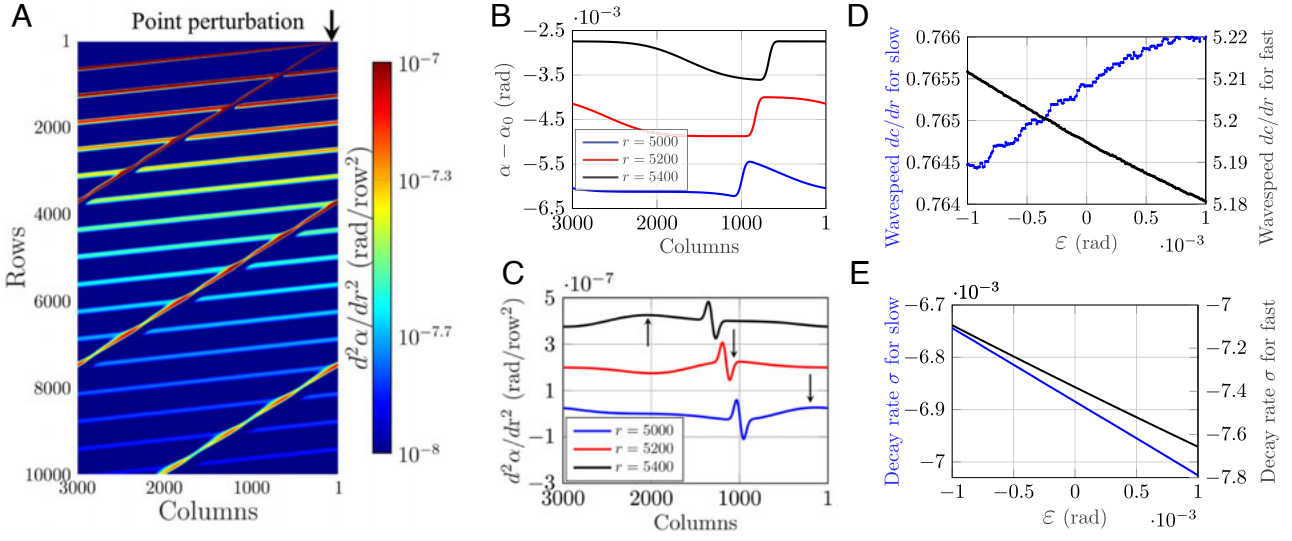

Fig. 5. Formation of two solitary waves resulting from a point perturbation at the edge of an a_2 polarized Maxwell lattice and their collisions. The lattice has $\alpha_0 = 1.3144$ rad, and the point perturbation is applied to the *Top* row at column 50. (*A–C*) Perturbation amplitude $\varepsilon = 0.23$ mrad. (*A*) $d^2\alpha/dr^2$ as a function of space. (*B*) $\alpha - \alpha_0$ and (*C*) $d^2\alpha/dr^2$ for rows 5,000 (blue), 5200 (red), and 5,400 (black). Rows 5,200 and 5,400 are sequentially offset by 1.25 mrad in (*B*) and 0.2 μrad/(unit cell)^2 for visualization purposes. The black arrows point to the fast-moving, spatially wider, solitary wave. (*D*) "Speed" dc/dr of the solitary waves as a function of ε. (*E*) Decay rate of the peak-to-peak magnitude of $d^2\alpha/dr^2$ of the solitary waves σ, defined $\frac{d^2\alpha}{dr^2}_{max} - \frac{d^2\alpha}{dr^2}_{min} = Ae^{\sigma r}$.

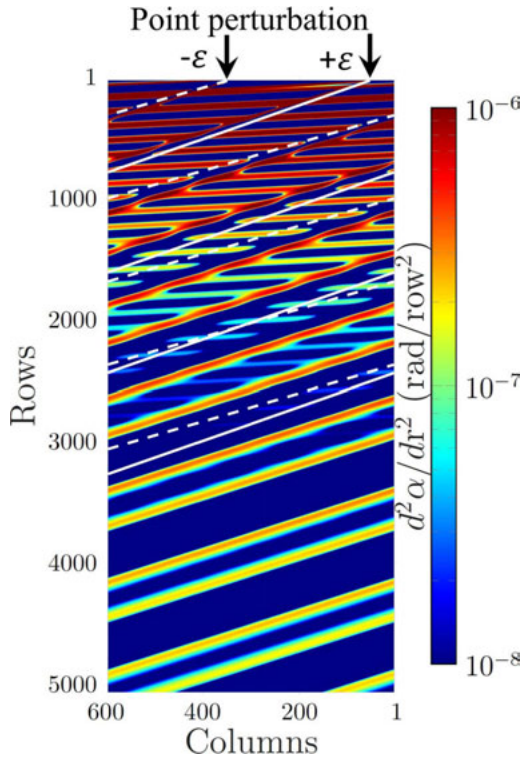

Fig. 6. Repulsion between two solitary waves, visualized via $\mathbf{d^2\alpha/dr^2}$, for two point perturbations applied to the soft edge (*Top*) of a lattice with the same homogeneous angle as in Fig. 5. Perturbations of $\pm\varepsilon = 0.6$ mrad are applied at columns 50 and 350, respectively. The solid and dashed lines demonstrate the predicted behavior of their perspective perturbations, respectively, based on the speeds calculated in *SI Appendix*.

Augmenting the complexity of the two solitary waves generated from a single point perturbation in the examples of Fig. 5, we simulate the response of the TMM to two point perturbations of differing signs (Fig. 6). As can be expected from the prior results, four solitary waves are generated; however, here, we see the unexpected phenomenon that the two long-lived solitary waves appear to repel one another and propagate with similar speeds thereafter. This change of behavior can be seen by comparing the intersection of their predicted trajectories calculated from the single perturbation case (shown in *SI Appendix*, Figs. S10 and S11), which are denoted by the dashed and solid white lines. Although the predicted trajectories intersect after about 2000 rows, the solitary like waves in the actual response never intersect, suggesting there is some form of repulsion between the two slow solitary-like waves. Such repulsion has been seen for solitary waves in other nonlinear systems, for instance, that of two kinks or two antikinks (topological solitons) in Sine-Gordon systems (36, 77) or optical spatial solitons (78).

Experimental Validation. To validate the numerical simulation results, we built physical models composed of laser-cut acrylic triangles pinned together such that they are free to rotate. The experimental lattice has a prescribed fixed perturbation on the top of the lattice, periodic boundary conditions on the left and right sides, and a free boundary condition on the bottom. Periodic boundary conditions are set by taking the α values for the first and last columns from the numerical simulations and pinning the left and right edge triangles to positions to match them. The perturbation is prescribed at the top of the lattice in a similar manner by fixing the top triangles. The resulting bulk configuration is found by taking a picture of the resulting lattice and using image processing to locate each hinge of the lattice and the resulting α, θ, and γ angles are calculated from those locations. More details of the image processing algorithm can be found in *SI Appendix*, Note 7. In Fig. 7, we show two lattice configurations with different-sized unit cells (31.5 [mm] and 40 [mm] along the longest sides $c_{r,b}$) under two different perturbations, a harmonic perturbation Fig. 7 *A–D* and a point perturbation Fig. 7 *E–H*). The lattice configuration is purely geometric and theoretically scale independent. In practice, manufacturing limitations such as the size of the hinge used put a lower limit on the unit cell size. Recent research has shown, however, that rotating features at the microscale are achievable through advanced 3D printing techniques (79). The error between the experimental and numerical lattices is found by taking the difference between the experimental α value of each unit cell α_{exp} and the numerically solved α value α_{sim} and

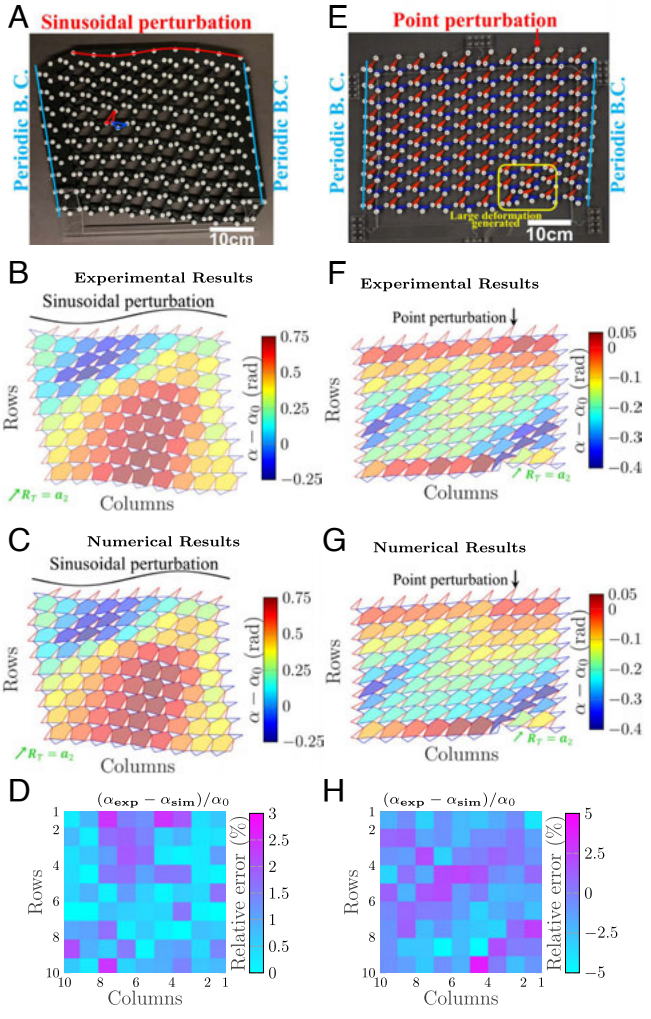

Fig. 7. Physical realization of $\mathbf{a_2}$ polarized Maxwell lattices with laser-cut triangles, pinned hinges, and three prescribed boundaries, along with a comparison to numerical predictions. (*A–D*) Sinusoidal perturbation for $\alpha_0 = 1.3144$, $\varepsilon = 0.1$ rad, $k_x = 0.6283$ rad/unit cell. (*E–H*) Point perturbation for $\alpha_0 = 1.3144$ rad, $\varepsilon = 45$ mrad applied at column 3. (*A* and *E*) Photographs of the deformed lattice, where the left and right boundaries are prescribed to follow the computed periodic boundary configuration, (*B* and *F*) measured angles, and (*C* and *G*) simulated angles. (*D* and *G*) Percent differences between experiment (*B* and *E*) and simulation (*C* and *F*).

normalizing it by the homogeneous α value α_0. The error for both experiments was very small with a maximum error of less than 5%, as seen in Fig. 7 *D* and *H*. This error is due to the precision of the fit between the triangular unit cells and the pins used. Additionally, we note that in our experimental realization for the configuration showing the solitary wave propagation Fig. 7 *E*–*H*, multiple unit cells with θ angles close to π with sufficient pressure can be forced to snap from concave to convex configurations with the given prescribed boundaries as well as slight variability in the experimental configuration due to manufacturing tolerances of the hinges.

Discussion

The two central contributions of this work are i) demonstrating, to the linear order, that the ZMs of 2D TMMs (Maxwell lattices) can be mapped to waves in 1D non-Hermitian, nonreciprocal, dynamical systems; and ii) extending the study of 2D TMMs to the nonlinear regime and exploring the interplay therein with topological nontriviality. Within that scope, we showed that an array of nonlinear wave-like phenomena exists, including harmonic generation, localized topological domain switching, amplification-enhanced frequency conversion, and solitary wave generation. Each of these phenomena has its own unique implications for designing stress and deformation fields in materials that extends significantly past what has hitherto been achievable in linear regimes of TMMs, and, more broadly, via elasticity. Among these, localized intrinsic domain formation has the potential to tailor regions of SSSs with implications to fracture mechanics (75), and solitary wave generation has implications for compact, amplitude-dependent spatially addressable signal transmission (80) and remote-controlled localization of stress and deformation, both of which may find interesting use in the context of mechanoresponsive metamaterials (81). In the context of the analogy to the 1D spatiotemporal system, these 2D lattices offer a convenient emulator for nonlinear waves and share similarities with the mapping between d-dimensional quantum systems with $(d + 1)$-dimensional classical systems, which led to important advances in understanding quantum phase transitions (61). Finally, we envision a potentially intriguing scenario stemming from this work, wherein elasticity and inertial effects are incorporated into the lattice, such that perturbations are restricted by the underlying topology of the lattice as shown herein, but evolve in time.

Materials and Methods

The fabricated lattice structures are created by laser cutting (using a Glowforge Basic 3D laser cutter) 1/8-inch-thick acrylic layers assembled with barrels (Fig. 7*A*) or dowel pins (Fig. 7*E*) and screws. For the experiment in Fig. 7*A*, each of the barrels (6063 Aluminum Low-Profile Binding Barrels from McMaster-Carr) has a diameter of 13/64 inch and length of 1/4 inch (3/8 inch at the boundaries due to an extra layer of acrylic for prescribed periodic left–right boundary condition). For the experiment in Fig. 7*E*, each of the dowel pins (Alloy Steel Pull-Out Dowel Pin from McMaster-Carr) has a diameter of 1/4 inch and a length of 1/2 inch. Geometries of triangle unit cells are shown in *SI Appendix*, Figs. S12 and S13. The lattices are assembled by pinning down the triangles in two layers and to the laser-cut acrylic boundaries. Left and right boundaries are connected at the bottom of the lattice without interfering with the bottom row of triangles. Boundary pieces are connected using M3 screws and nuts.

Data, Materials, and Software Availability. All data generated or analyzed during this study are included in this published article (and its *SI Appendix*). All related codes are uploaded to GitHub: https://github.com/xiuhaning/2D_TMM_geometry_solutions.

ACKNOWLEDGMENTS. We thank N. Gravish for useful discussions regarding active systems. Funding: H.L., K.Q., S.S., N.B., and X.M. acknowledge support from the US Army Research Office (grant no. W911NF-20-2-0182). I.F. acknowledges support from the Department of Defense (DoD) through the National Defense Science & Engineering Graduate (NDSEG) Fellowship Program. B.M. acknowledges support from the US Department of Energy (DOE) National Nuclear Security Administration (NNSA) Laboratory Graduate Residency Fellowship (LRGF) under Cooperative Agreement DE-NA0003960. H.X., Z.C., and X.M. acknowledge support from the Office of Naval Research (grant no. ONR MURI N00014-20-1-2479).

Author affiliations: [a]Department of Surgery, Brigham and Women's Hospital/Harvard Medical School, Boston, MA 02115; [b]Department of Mechanical and Aerospace Engineering, University of California San Diego, La Jolla, CA 92093; and [c]Department of Physics, University of Michigan, Ann Arbor, MI 48109

Author contributions: Z.C., N.B., and X.M. designed research; H.X., I.F., H.L., K.Q., S.S., B.M., Z.C., N.B., and X.M. performed research; H.X., I.F., H.L., and K.Q. analyzed data; and H.X., I.F., H.L., K.Q., S.S., Z.C., N.B., and X.M. wrote the paper.

1. M. Z. Hasan, C. L. Kane, Colloquium: Topological insulators. *Rev. Mod. Phys.* **82**, 3045 (2010).
2. F. Zangeneh-Nejad, A. Alù, R. Fleury, Topological wave insulators: A review. *Comptes Rendus. Phys.* **21**, 467–499 (2020).
3. X. L. Qi, S. C. Zhang, Topological insulators and superconductors. *Rev. Mod. Phys.* **83**, 1057–1110 (2011).
4. J. K. Asbóth, L. Oroszlány, A. Pályi, A short course on topological insulators: Band structure and edge states in one and two dimensions. *Lect. Notes Phys.* **919**, 166 (2016).
5. C. Beenakker, L. Kouwenhoven, A road to reality with topological superconductors. *Nat. Phys.* **12**, 618–621 (2016).
6. D. Aasen *et al*., Milestones toward Majorana-based quantum computing. *Phys. Rev. X* **6**, 031016. (2016).
7. C. Tutschku, R. W. Reinthaler, C. Lei, A. H. MacDonald, E. M. Hankiewicz, Majorana-based quantum computing in nanowire devices. *Phys. Rev. B* **102**, 125407. (2020).
8. M. J. Gilbert, Topological electronics. *Commun. Phys.* **4**, 1–12 (2021).
9. H. Chorsi *et al*., Topological materials for functional optoelectronic devices. *Adv. Funct. Mater.* **32**, 2110655 (2022).
10. Z. Yang *et al*., Topological acoustics. *Phys. Rev. Lett.* **114**, 114301. (2015).
11. X. Li, S. Yu, H. Liu, M. Lu, Y. Chen, Topological mechanical metamaterials: A brief review. *Curr. Opin. Solid State Mater. Sci.* **24**, 100853. (2020).
12. S. D. Huber, Topological mechanics. *Nat. Phys.* **12**, 621–623 (2016).
13. K. Bertoldi, V. Vitelli, J. Christensen, M. Van Hecke, Flexible mechanical metamaterials. *Nat. Rev. Mater.* **2**, 1–11 (2017).
14. N. Singh, M. van Hecke, Design of pseudo-mechanisms and multistable units for mechanical metamaterials. *Phys. Rev. Lett.* **126**, 248002. (2021).
15. W. P. Su, J. R. Schrieffer, A. J. Heeger, Solitons in polyacetylene. *Phys. Rev. Lett.* **42**, 1698–1701 (1979).
16. C. Kane, T. Lubensky, Topological boundary modes in isostatic lattices. *Nat. Phys.* **10**, 39–45 (2014).
17. D. Rocklin, S. Zhou, K. Sun, X. Mao, Transformable topological mechanical metamaterials. *Nat. Commun.* **8**, 1–9 (2017).
18. J. Paulose, B. Gg. Chen, V. Vitelli, Topological modes bound to dislocations in mechanical metamaterials. *Nat. Phys.* **11**, 153–156 (2015).
19. K. Sun, A. Souslov, X. Mao, T. Lubensky, Surface phonons, elastic response, and conformal invariance in twisted Kagome lattices. *Proc. Natl. Acad. Sci. U.S.A.* **109**, 12369–12374 (2012).
20. T. Lubensky, C. Kane, X. Mao, A. Souslov, K. Sun, Phonons and elasticity in critically coordinated lattices. *Rep. Progr. Phys.* **78**, 073901. (2015).
21. H. Zhang, J. Wu, D. Fang, Y. Zhang, Hierarchical mechanical metamaterials built with scalable tristable elements for ternary logic operation and amplitude modulation. *Sci. Adv.* **7**, eabf1966 (2021).
22. D. Zhou, J. Ma, K. Sun, S. Gonella, X. Mao, Switchable phonon diodes using nonlinear topological maxwell lattices. *Phys. Rev. B* **101**, 104106. (2020).
23. J. L. Silverberg *et al*., Origami structures with a critical transition to bistability arising from hidden degrees of freedom. *Nat. Mater.* **14**, 389–393 (2015).
24. W. Zunker, S. Gonella, Soft topological lattice wheels. *Extreme Mech. Lett.* **46**, 101344. (2021).
25. J. McInerney, B. G. ge Chen, L. Theran, C. D. Santangelo, D. Z. Rocklin, Hidden symmetries generate rigid folding mechanisms in periodic origami. *Proc. Natl. Acad. Sci. U.S.A.* **117**, 30252–30259 (2020).
26. A. Bossart, D. M. Dykstra, J. Van der Laan, C. Coulais, Oligomodal metamaterials with multifunctional mechanics. *Proc. Natl. Acad. Sci. U.S.A.* **118**, e2018610118. (2021).
27. O. R. Bilal, R. Süsstrunk, C. Daraio, S. D. Huber, Intrinsically polar elastic metamaterials. *Adv. Mater.* **29**, 1700540 (2017).
28. X. Mao, T. C. Lubensky, Maxwell lattices and topological mechanics. *Annu. Rev. Condens. Matter Phys.* **9**, 413–433 (2018).
29. D. Z. Rocklin, Directional mechanical response in the bulk of topological metamaterials. *New J. Phys.* **19**, 065004. (2017).

30. B. Gg. Chen, N. Upadhyaya, V. Vitelli, Nonlinear conduction via solitons in a topological mechanical insulator. *Proc. Natl. Acad. Sci. U.S.A.* **111**, 13004–13009 (2014).
31. P. W. Lo *et al*., Topology in nonlinear mechanical systems. *Phys. Rev. Lett.* **127**, 076802. (2021).
32. G. U. Patil, K. H. Matlack, Review of exploiting nonlinearity in phononic materials to enable nonlinear wave responses. *Acta Mech.* **233**, 1–46 (2021).
33. M. Lapine IV, YS Kivshar. Shadrivov, Colloquium: Nonlinear metamaterials. *Rev. Mod. Phys.* **86**, 1093 (2014).
34. A. Scott, *Encyclopedia of Nonlinear Science* (Routledge, 2006).
35. Z. Chen, M. Segev, D. N. Christodoulides, Optical spatial solitons: Historical overview and recent advances. *Rep. Progr. Phys.* **75**, 086401. (2012).
36. T. Dauxois, M. Peyrard, *Physics of Solitons* (Cambridge University Press, 2006).
37. R. W. Boyd, *Nonlinear Optics* (Academic Press, 2020).
38. A. H. Nayfeh, D. T. Mook, *Nonlinear Oscillations* (John Wiley & Sons, 2008).
39. S. H. Strogatz, *Nonlinear Dynamics and Chaos: With Applications to Physics, Biology, Chemistry, and Engineering* (CRC Press, 2018).
40. B. M. Manda, R. Chaunsali, G. Theocharis, C. Skokos, Nonlinear topological edge states: From dynamic delocalization to thermalization. *Phys. Rev. B* **105**, 104308 (2022).
41. D. Smirnova, D. Leykam, Y. Chong, Y. Kivshar, Nonlinear topological photonics. *Appl. Phys. Rev.* **7**, 021306 (2020).
42. R. Chaunsali, H. Xu, J. Yang, P. G. Kevrekidis, G. Theocharis, Stability of topological edge states under strong nonlinear effects. *Phys. Rev. B* **103**, 024106. (2021).
43. J. R. Tempelman, K. H. Matlack, A. F. Vakakis, Topological protection in a strongly nonlinear interface lattice. *Phys. Rev. B* **104**, 174306. (2021).
44. N. Pernet *et al*., Gap solitons in a one-dimensional driven-dissipative topological lattice. *Nat. Phys.* **18**, 678–684 (2022).
45. D. Zhou, D. Rocklin, M. Leamy, Y. Yao, Topological invariant and anomalous edge modes of strongly nonlinear systems. *Nat. Commun.* **13**, 1–9 (2022).
46. C. Chong, M. A. Porter, P. G. Kevrekidis, C. Daraio, Nonlinear coherent structures in granular crystals. *J. Phys.: Condens. Matter* **29**, 413003 (2017).
47. L. Thatcher, P. Fairfield, L. Merlo-Ramírez, J. M. Merlo, Experimental observation of topological phase transitions in a mechanical 1D-SSH model. *Phys. Scripta* **97**, 035702. (2022).
48. V. Nesterenko, *Dynamics of Heterogeneous Materials* (Springer Science & Business Media, 2013).
49. D. Marković, A. Mizrahi, D. Querlioz, J. Grollier, Physics for neuromorphic computing. *Nat. Rev. Phys.* **2**, 499–510 (2020).
50. A. S. Raja *et al*., Ultrafast optical circuit switching for data centers using integrated soliton microcombs. *Nat. Commun.* **12**, 1–7 (2021).
51. T. J. Kippenberg, A. L. Gaeta, M. Lipson, M. L. Gorodetsky, Dissipative kerr solitons in optical microresonators. *Science* **361**, eaan8083 (2018).
52. R. El-Ganainy *et al*., Non-Hermitian physics and PT symmetry. *Nat. Phys.* **14**, 11–19 (2018).
53. Y. Ashida, Z. Gong, M. Ueda, Non-Hermitian physics. *Adv. Phys.* **69**, 249–435 (2020).
54. D. L. Sounas, A. Alù, Non-reciprocal photonics based on time modulation. *Nat. Photonics* **11**, 774–783 (2017).
55. B. I. Popa, S. A. Cummer, Non-reciprocal and highly nonlinear active acoustic metamaterials. *Nat. Commun.* **5**, 3398 (2014).
56. A. Maznev, A. Every, O. Wright, Reciprocity in reflection and transmission: What is a 'phonon diode'? *Wave Motion* **50**, 776–784 (2013).
57. W. Yao, W. Zhong, C. W. Lim, *Symplectic Elasticity* (World Scientific, 2009).
58. J. Sui, J. Chen, X. Zhang, G. Nie, T. Zhang, Symplectic analysis of wrinkles in elastic layers with graded stiffnesses. *J. Appl. Mech.* **86**, 011008. (2019).
59. Q. Wu, Q. Gao, The symplectic approach for analytical solution of micropolar plane stress problem. *Int. J. Solids Struct.* 112095 (2022).
60. P. Gd. Gennes, Soluble model for fibrous structures with steric constraints. *J. Chem. Phys.* **48**, 2257–2259 (1968).
61. S. L. Sondhi, S. M. Girvin, J. P. Carini, D. Shahar, Continuous quantum phase transitions. *Rev. Mod. Phys.* **69**, 315–333 (1997).
62. B. H. Kolner, Space-time duality and the theory of temporal imaging. *IEEE J. Quantum Electron.* **30**, 1951–1963 (1994).
63. F. Wilczek, Quantum time crystals. *Phys. Rev. Lett.* **109**, 160401. (2012).
64. C. Chong, P. G. Kevrekidis, *Coherent Structures in Granular Crystals: From Experiment and Modelling to Computation and Mathematical Analysis* (Springer, 2018).
65. S. Xia *et al*., Nonlinear tuning of PT symmetry and non-Hermitian topological states. *Science* **372**, 72–76 (2021).
66. M. C. Cross, P. C. Hohenberg, Pattern formation outside of equilibrium. *Rev. Mod. Phys.* **65**, 851 (1993).
67. N. Akhmediev, A. Ankiewicz, *Dissipative Solitons: From Optics to Biology and Medicine* (Springer Science & Business Media, 2008), vol. 751.
68. C. R. Calladine, Buckminster fuller's "tensegrity" structures and clerk maxwell's rules for the construction of stiff frames. *Int. J. Solids Struct.* **14**, 161–172 (1978).
69. S. Guest, J. Hutchinson, On the determinacy of repetitive structures. *J. Mech. Phys. Solids* **51**, 383–391 (2003).
70. Y. Zheng, I. Niloy, P. Celli, I. Tobasco, P. Plucinsky, Continuum field theory for the deformations of planar Kirigami. *Phys. Rev. Lett.* **128**, 208003. (2022).
71. M. Moshe *et al*., Nonlinear mechanics of thin frames. *Phys. Rev. E* **99**, 013002. (2019).
72. M. Czajkowski, C. Coulais, M. van Hecke, D. Rocklin, Conformal elasticity of mechanism-based metamaterials. *Nat. Commun.* **13**, 1–9 (2022).
73. Y. Zheng, I. Tobasco, P. Celli, P. Plucinsky, Modeling planar Kirigami metamaterials as generalized elastic continua. Soft Condens. Matter, arXiv [Preprint] (2022). http://arxiv.org/abs/2206.00153.
74. M. Czajkowski, D. Rocklin, Duality and sheared analytic response in mechanism-based metamaterials. Soft Condensed Matter, arXiv [Preprint] (2022). http://arxiv.org/abs/2205.10751.
75. L. Zhang, X. Mao, Fracturing of topological maxwell lattices. *New J. Phys.* **20**, 063034. (2018).
76. N. J. Zabusky, M. D. Kruskal, Interaction of "solitons" in a collisionless plasma and the recurrence of initial states. *Phys. Rev. Lett.* **15**, 240 (1965).
77. N. Gao, K. Lu, An underwater metamaterial for broadband acoustic absorption at low frequency. *Appl. Acoust.* **169**, 107500. (2020).
78. G. I. Stegeman, M. Segev, Optical spatial solitons and their interactions: Universality and diversity. *Science* **286**, 1518–1523 (1999).
79. J. C. Williams, H. Chandrahalim, J. S. Suelzer, N. G. Usechak, Multiphoton nanosculpting of optical resonant and nonresonant microsensors on fiber tips. *ACS Appl. Mater. Interfaces* **14**, 19988–19999, PMID: 35412300 (2022).
80. B. Garbin, J. Javaloyes, G. Tissoni, S. Barland, Topological solitons as addressable phase bits in a driven laser. *Nat. Commun.* **6**, 1–7 (2015).
81. M. A. Ghanem *et al*., The role of polymer mechanochemistry in responsive materials and additive manufacturing. *Nat. Rev. Mater.* **6**, 84–98 (2021).